# Finite-Control-Set Model-Predictive Control of Open-End Winding Synchronous Reluctance Motor Drives

1st Filippo Gemma
*Electrical, Computer and Biomedical Engineering Dept*
*University of Pavia*
Pavia, IT
filippo.gemma01@universitadipavia.it

2nd Jacopo Riccio
*Power electronics, machines and control group*
*University of Nottingham*
Nottingham, UK
Jacopo.Riccio2@nottingham.ac.uk

3rd Giulia Tresca
*Electrical, Computer and Biomedical Engineering Dept*
*University of Pavia*
Pavia, IT
giulia.tresca@unipv.it

4th Oriana Benfatto
*Electrical, Computer and Biomedical Engineering Dept*
*University of Pavia*
Pavia, IT
oriana.benfatto01@universitadipavia.it

5th Pericle Zanchetta
*Electrical, Computer and Biomedical Engineering Dept*
*University of Pavia*
Pavia, IT
pericle.zanchetta@unipv.it

***Abstract*—This paper presents a novel control strategy for a Synchronous Reluctance Machine (SyRel) in an Open-End Winding (OEW) configuration. The proposed approach employs Finite Control Set Model Predictive Control (FCS-MPC) to handle the multi-variable nature of the system, enabling the coordinated control of two converters through a unified cost function. The control strategy is built upon an experimentally derived magnetic model of the machine, allowing the exploitation of the machine's inherent non-linearity within the control scheme. The developed method ensures high dynamic performance and achieves key objectives such as a unity power factor on the main side, an extended constant torque region (CTR) with the same current rating, and fast response in both current and voltage control. Simulation results validate the effectiveness of the proposed strategy, highlighting its potential for SyRel applications.**

***Index Terms*—Synchronous Reluctance Motor, Two-Level Voltage Source Inverter, Open-End Winding, Floating Capacitor, Finite Control Set Model Predictive Control.**

## I. Introduction

Synchronous reluctance (SyRel) motor drives are compelling alternatives to induction and permanent magnet synchronous motor drives in a wide spectrum of applications [1]. This broad application uptake can be attributed to their high dynamic performance, good power density, competitive costs, and reduced environmental impact due to the lack of rare earth permanent magnet materials [2]. However, despite their economic advantages, SyRel motor drives face notable challenges, including a low power factor, a limited constant power speed range, significant torque ripple, and highly non-linear magnetic characteristics that complicate the control strategy.

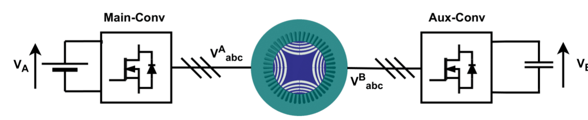


Fig. 1. SyRel in OEW with FC drive scheme.

A promising strategy to enhance the constant power speed range and improve the power factor of SyRel drives involves utilizing a SyRel machine with an open-end winding (OEW) configuration, where each winding end is connected to a three-phase voltage source inverter [3]. This approach increases the voltage at the motor terminals and leverages the inherent multilevel voltage output capability, enabling enhanced control over torque and speed. Additionally, the OEW features fault tolerance [4], as the system can maintain operation by rerouting currents through unaffected sections, thereby enhancing the overall reliability and robustness of the motor drive.

Fig. 1 illustrates the described system, where both ends of the machine's windings are fed by a main converter (Main-Conv) and an auxiliary converter (Aux-Conv). The literature identifies three distinct configurations based on how the auxiliary converter's DC-link is connected: 1) a shared DC-link between the two inverters [5]; 2) two independent DC-links with separate supplies [6]; 3) a floating capacitor (FC) connected to the Aux-Conv's DC-link [7].

While the common DC-bus topology offers advantages such as a compact design, a high torque per volume ratio, and fault tolerance, challenges arise due to the presence of zero-sequence current [8]. Either the converter's output Common

Mode Voltage is eliminated by employing a more complex modulation strategy and reduced input/output voltage transfer ratio or additional system losses and increased torque ripple arise [9]. In contrast, the dual isolated DC-link configuration avoids zero-sequence current circulation but, as in standard VSI systems, can generate a common-mode voltage that induces shaft voltage and bearing currents, reducing the drive's lifespan [10]. The FC-based solution, on the other hand, eliminates the zero-sequence current problem and provides the added advantage of adjusting the FC voltage during operation to improve the torque-speed characteristic [7]. Specifically, increasing the FC voltage extends the constant-torque region and delays field-weakening operations [11]. The voltage ratio between the two DC buses plays a crucial role in influencing DC-link voltage utilization and torque-speed characteristics. While previous research has focused on optimizing the torque-speed curve by relaxing the power factor constraints in induction motors [12], or analyzing single voltage ratios [13], the potential of fine-tuning the FC voltage level to enhance SyRel motor drive performance remains largely unexplored.

In this paper, the FC DC bus becomes a state variable and needs to be controlled, with its charging facilitated by the current flowing through the SyRel motor from the Main-Conv to the Aux-Conv. The first tool used in this work is the experimental characterization of the SyRel motor's magnetic model under test conditions. The first contribution involves the design of a finite-control set model predictive control (FCS-MPC) [14], which simultaneously regulates the SyRel motor current vector and the FC voltage level within a single control loop, while also compensating for the reactive power of the Main-Conv. Employing FCS-MPC becomes particularly effective for controlling systems with numerous state variables and multiple constraints, as demonstrated in previous studies [15].

## II. Magnetic Model Experimental Characterization and SI Drive Operations

The defining equations of a SyRel machine can be expressed in the $dq$ rotating reference frame as follows [16]:

$$v_{s,dq} = R_s i_{dq} + L\frac{di_{dq}}{dt} - Qw_r\phi_{dq} \tag{1}$$

$$\boldsymbol{L} = \begin{bmatrix} L_{dd}\left(i_d, i_q\right) & L_{dq}\left(i_d, i_q\right) \\ L_{qd}\left(i_d, i_q\right) & L_{qq}\left(i_d, i_q\right) \end{bmatrix} \tag{2}$$

$$\boldsymbol{Q} = \begin{bmatrix} 0 & -1 \\ 1 & 0 \end{bmatrix} \tag{3}$$

$$T_{em} = \frac{3}{2}p\left(\phi_{dq} \;\; x \;\; i_{dq}\right) \tag{4}$$

where $v_s$ is the stator machine voltage, $\phi_d$, $\phi_q$, $i_d$, and $i_q$ represent the inductances, fluxes, and currents along the $d$- and $q$-axes, respectively; $T_{em}$ denotes the electromagnetic torque; $\omega_r$ is the rotor's electrical speed, $R_s$ is the stator resistance, and $p$ is the pole pair count; $\boldsymbol{L}$ is the incremental matrix, and $\boldsymbol{Q}$ represents an orthogonal rotation matrix. The components

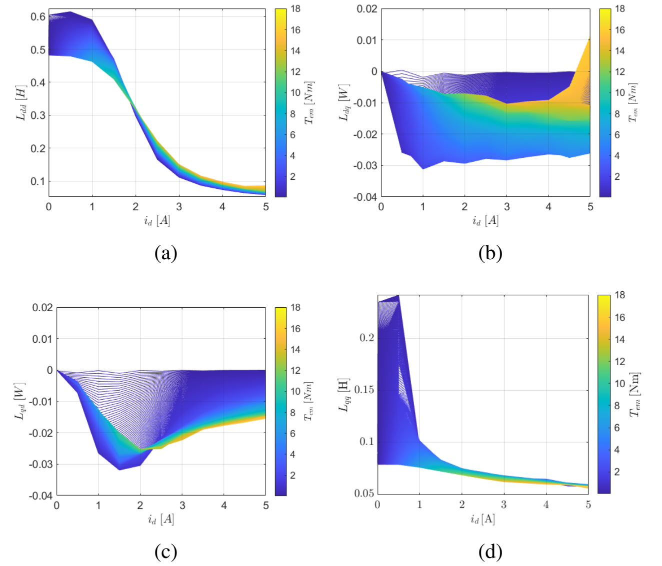

Fig. 2. Experimental incremental inductances: (a) $L_{dd}$, (b) $L_{dq}$, (c) $L_{qd}$, (d) $L_{qq}$

of $\boldsymbol{L}$ can be numerically evaluated from the flux linkages and the current components as:

$$L_{dd} = \frac{\partial \phi_d}{\partial i_d} \approx \frac{\phi_{d+1}^q - \phi_d^q}{\Delta i} \tag{5a}$$

$$L_{qq} = \frac{\partial \phi_q}{\partial i_q} \approx \frac{\phi_{q+1}^{d+1} - \phi_q^d}{\Delta i} \tag{5b}$$

$$L_{dq} = \frac{\partial \phi_d}{\partial i_q} \approx \frac{\phi_{d+1}^{q+1} - \phi_d^q}{\Delta i} \tag{5c}$$

$$L_{qd} = \frac{\partial \phi_q}{\partial i_d} \approx \frac{\phi_{q+1}^d - \phi_q^d}{\Delta i}. \tag{5d}$$

In (5), the term "$\Delta i$" is the fixed current step corresponding to two consecutive magnetic flux points. Subscripts identify the flux map, and superscripts denote to which orthogonal current a specific map is referred. The terms $L_{dd}$ and $L_{qq}$ are the direct and quadrature incremental inductance components respectively, shown in Fig. 2(a) and 2(d). The quantities $L_{dq}$ and $L_{qd}$ are the cross magnetization inductance, resulting in non-zero terms, presented in Fig. 2(b) and 2(c).

A key characteristic of the SyRel motor is its non-linear relationship between flux and current, primarily influenced by self-axis and cross-saturation effects [16]. Self-axis saturation arises when the direct and quadrature current components individually saturate their corresponding flux components. Cross-saturation, on the other hand, results in variations in the direct flux due to quadrature current changes and vice versa. Thus, the $d$- and $q$-flux components must be modeled as non-linear functions of the current vector, i.e., $\phi_d(i_d, i_q)$ and $\phi_q(i_d, i_q)$.

A widely recognized method to determine the flux-versus-current maps for the SyRel motor is outlined in [17]. This method has been employed here to identify the $\phi_d$ and $\phi_q$ characteristics, that are used in the FCS-MPC for an accurate

TABLE I
NAMEPLATE PARAMETERS OF THE SYREL MOTOR UNDER TEST.

| Variable | Symbol | Value | Unit |
|---|---|---|---|
| Stator Resistance | $R_s$ | 6.3 | Ω |
| Rated Torque | $T_{em}$ | 7 | Nm |
| Rated Speed | $\omega_m$ | 1500 | rpm |
| Rated Power | $P_n$ | 1.1 | kW |
| Rated Current (RMS) | $I_n$ | 4.1 | A |
| Rated Voltage (RMS) | $V_n$ | 380 | V |
| Pole Pairs | $p$ | 2 | # |

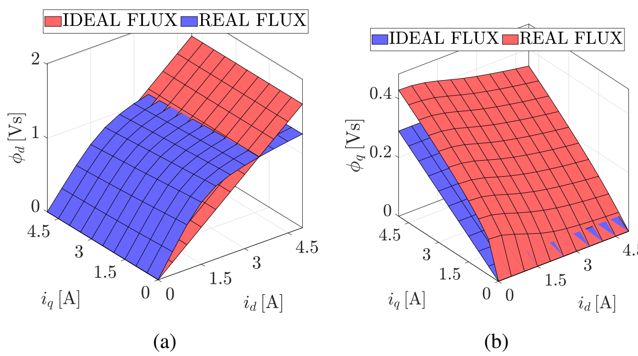


Fig. 3. Experimental flux maps: (a) $d$-flux and (b) $q$-flux characteristics.

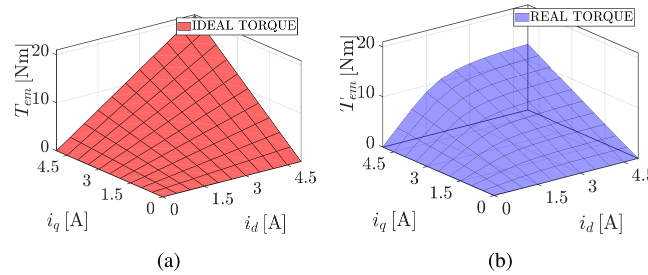


Fig. 4. Electromagnetic torque results: (a) ideal, (b) experimental.

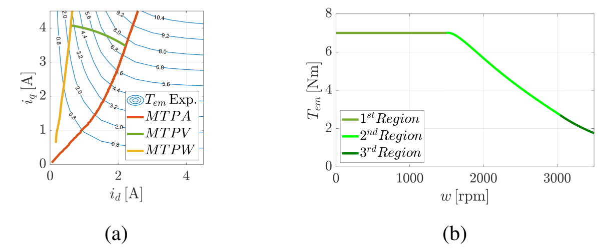


Fig. 5. Experimental results: (a) $i_d, i_q$-plane real SI trajectories (MTPA, MTPV, MTPW). (b) Torque-speed characteristics for the real SI configuration.

system prediction, in combination with (5). The motor's parameters are listed in Tab. I. The experimental process involves setting a specific PM rotational speed while controlling the SyRel in current control mode across several operating points in the $d$- and $q$-current domains.

The experimentally obtained $\phi_d$ and $\phi_q$ characteristics are presented in Fig. 3(a) and 3(b), respectively, alongside the linear magnetic characteristics for comparison. From these flux maps, the ideal and experimental electromagnetic torque, represented as $T_{em}$, are calculated and shown in Fig. 4(a) and 4(b).

Having detailed the flux and torque maps in the $dq$ current plane, control trajectories for a SyRel drive system with a 2-level VSI powered by a fixed DC voltage source can be derived. Assumptions include negligible stator resistance, no iron losses, and ideal converter operation. The optimal control trajectories, such as maximum torque per ampere (MTPA) and maximum torque per weber (MTPW), are derived numerically and illustrated using isotorque curves in Fig. 5(a). The analysis identifies the constant torque region (CTR), which operates below the base speed ($w_b^{SI} = 1500$ rpm). Fig. 5(b) highlights the torque-versus-speed characteristics, showing maximum torque in the CTR and a reduction in torque during flux-weakening. To mitigate torque loss at high speeds, the second flux-weakening region introduces an MTPW trajectory for the current vector.

## III. SYSTEM MODEL

### A. Real OEW SyRel and Floating Bridge Capacitor Equations

The characteristic equations of an OEW SyRel drive system and a floating capacitor are hereafter presented. The schematic drive system topology is depicted in Fig. 1. The equations have been carried out at steady state considering the $dq$ coordinates synchronous with the SyRel current, assuming 1) negligible stator resistance; 2) ideal switching behavior of the converters; 3) iron losses neglected; and 4) non-linear magnetic characteristics, derived from the magnetic model outlined in Sec. II.

The SyRel stator voltage equation can be represented as follows:

$$\overline{v}_S = \overline{v}_A - \overline{v}_B \tag{6}$$

where $\overline{v}_S$, $\overline{v}_A$, and $\overline{v}_B$ are the voltage space vectors of the motor, main converter, and auxiliary converter, respectively. While considering the $dq$ frame, the stator SyRel voltages (i.e. $v_d$, $v_q$) can be expressed at steady state as:

$$v_d = v_{Ad} - v_{Bd} \tag{7a}$$

$$v_q = v_{Aq} - v_{Bq} \tag{7b}$$

where the DC- and the FC-side voltages are denoted by $v_{Ad}$, $v_{Aq}$, $v_{Bd}$, and $v_{Bq}$, respectively.

The voltage across the floating capacitor $C$ is related to its electrostatic energy, which varies at the following rate:

$$\frac{d}{dt}\left(\frac{1}{2}CV_B^2\right) = \frac{3}{2}\overline{i_S} \cdot \overline{v_B} \tag{8}$$

where $V_B$ is the DC-link voltage of the FC and "$\cdot$" is the dot product, calculated by summing the products of the corresponding $d$ and $q$ components of the first and second vector.

### B. Control Strategy

An FCS-MPC algorithm is based on predicting the future behavior of the system for each possible actuating command.

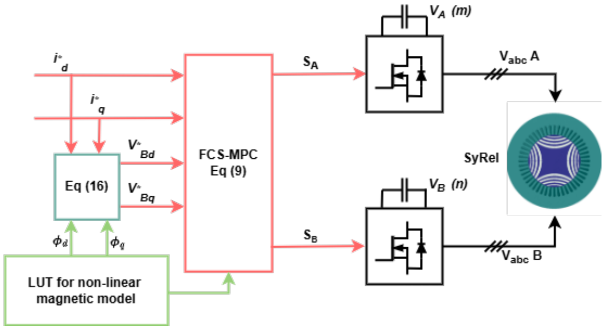


Fig. 6. Simplified proposed control scheme.

It then chooses the command that minimizes a given cost function, which is proportional to the error between predictions and references. A block diagram is depicted in Fig. 6.

The controller has been designed to ensure the tracking of the current vector and DC voltage on the FC, while also compensating for the reactive power of the Main-Conv and the active power of the Aux-Conv. A single cost function incorporates five reference tracking terms. Unlike conventional drive configured in OEW [15].

The system is modeled in a synchronous reference frame rotating at the electrical speed $\omega_r$. The cost function $g(m,n)$ is expressed as:

$$\begin{aligned} g = & \\ & \left\| \mathbf{i_{d,q}}^* - \mathbf{i_{d,q}}^{k+1}(m,n) + W_{i_{d,q}} T_s \left( \sum_{z=0}^{l} \mathbf{i_{d,q\ err}}^{k-z} \right) \right\|_2^2 \\ & + w_{V_B} \left[ V_B^* - \mathbf{V_B}^{k+1}(n) \right]^2 \\ & + w_{V_{Bd}} \left[ V_{Bd}^* - \mathbf{V_{Bd}}^{k+1}(n) \right]^2 \\ & + w_{V_{Bq}} \left[ V_{Bq}^* - \mathbf{V_{Bq}}^{k+1}(n) \right]^2 \end{aligned} \tag{9}$$

This function comprises the squared two-norm of the error between the reference current $\mathbf{i_{d,q}}^*$ and the predicted current $\mathbf{i_{d,q}}^{k+1}(m,n)$, the desired DC-link voltage on the B-side $V_B^*$ and its predicted counterpart $V_B^{k+1}(n)$, as well as the $d$- and $q$-axis FC voltage references and their respective predictions. The last two terms of (9) are soft constraints to guarantee the unity power factor on the main side.

The indices $m$ and $n$ correspond to the eight configurable switching states of the Main-Conv and Aux-Conv, respectively, resulting in 64 possible combinations. The pair $(m,n)$ that minimizes (9) is selected to apply to the system at the desired operating point in the next time step.

The current predictions are derived from the simplified SyRel drive model, which is discretized using the forward Euler approximation as follows [18]:

$$\begin{aligned} \boldsymbol{i}_{d,q}^{k+1}(m,n) = \boldsymbol{i}_{d,q}^{k} + T_s \boldsymbol{L}^{-1} \Big[ & \boldsymbol{v}_s(m,n) - R_s \boldsymbol{i}_{d,q}^{k} + \\ & + \boldsymbol{Q} \omega_r \boldsymbol{L} \boldsymbol{i}_{d,q}^{k} \Big] \end{aligned} \tag{10}$$

where $\boldsymbol{i}_{d,q}^{k}$ represents the measured current vector, $T_s$ is the sampling period and $\boldsymbol{L}^{-1}$ is the inverse matrix of $\boldsymbol{L}$. An integral action, represented by $W_{i_{d,q}} T_s \left( \sum_{z=0}^{l} i_{d,q\ err}^{k-z} \right)$, is included to enhance system robustness [19].

The prediction of the DC-link voltage for a three-phase system is computed as:

$$V_B^{k+1}(n) = V_B^k - \frac{3T_s}{4C} \left[ S_a(n) i_a + S_b(n) i_b + S_c(n) i_c \right] \tag{11}$$

Here, $V_B^k$ is the current B-side DC-link voltage measurement, with $C$ being the capacitance. The terms $S_a(n)$, $S_b(n)$, and $S_c(n)$ denote the on-state (one) or off-state (zero) of the switches, while $i_a$, $i_b$, and $i_c$ are the phase current components.

The $V_{Bd}^*$ and $V_{Bq}^*$ values are derived from a rotating reference frame synchronized with the stator current space vector $\overline{i_S}$. The output voltage of the floating bridge is given by:

$$\overline{v_B} = (v_B^p + j v_B^q) \frac{\overline{i_S}}{|\overline{i_S}|} \tag{12}$$

where $v_B^p$ and $v_B^q$ represent, respectively, the components of $\overline{v_B}$ that are parallel and orthogonal to $\overline{i_S}$. These components are proportional to the active and reactive power of the Aux-Conv [3]. In this reference frame, (8) transforms into:

$$\frac{d}{dt} \left( \frac{1}{2} C V_B^2 \right) = \frac{3}{2} |\overline{i_S}| \, v_B^p \tag{13}$$

This equation indicates that the rate of change of energy in the floating bridge, and consequently its voltage, can be regulated by adjusting the parallel component of $\overline{v_B}$. Hence, at steady state, $v_B^p$ is set to zero, and the reference value for the parallel component of the FC voltage is also set to zero.

The orthogonal component $v_B^q$ provides a degree of freedom for controlling the reactive power of the floating bridge inverter and more generally, the power factor of the DC link of the main side. The active power $P_A$ of inverter A must adhere to the voltage and current limits of the power source. The relationship between $P_A$ and the reactive power $Q_A$ is described by:

$$P_A^2 + Q_A^2 = \left( \frac{3}{2} |\overline{i_S}| \, |\overline{v_A}| \right)^2 \tag{14}$$

Under steady-state conditions, the active power $P_A$ accounts for Joule losses, and the mechanical power delivered to the motor (with the active power transferred to inverter B being negligible). The right-hand side of (14) represents the square of the apparent power of inverter A.

The reactive power $Q_A$ can be expressed as:

$$Q_A = \frac{3}{2} \overline{v_A} \cdot j \overline{i_B} = Q_S + Q_B \tag{15}$$

where $Q_S$ and $Q_B$ are the reactive power contributions of the SyRel and Inverter B, respectively.

By combining (1) and (15) under steady-state conditions, setting $Q_A$ to zero, and neglecting the voltage drop across the stator resistance, the optimal value of $v_B^{q\,*}$ is obtained as:

$$v_B^{q\,*} = -\frac{w_r^*}{|\overline{i_S^*}|} \left( \phi_d^* i_d^* + \phi_q^* i_q^* \right) \tag{16}$$

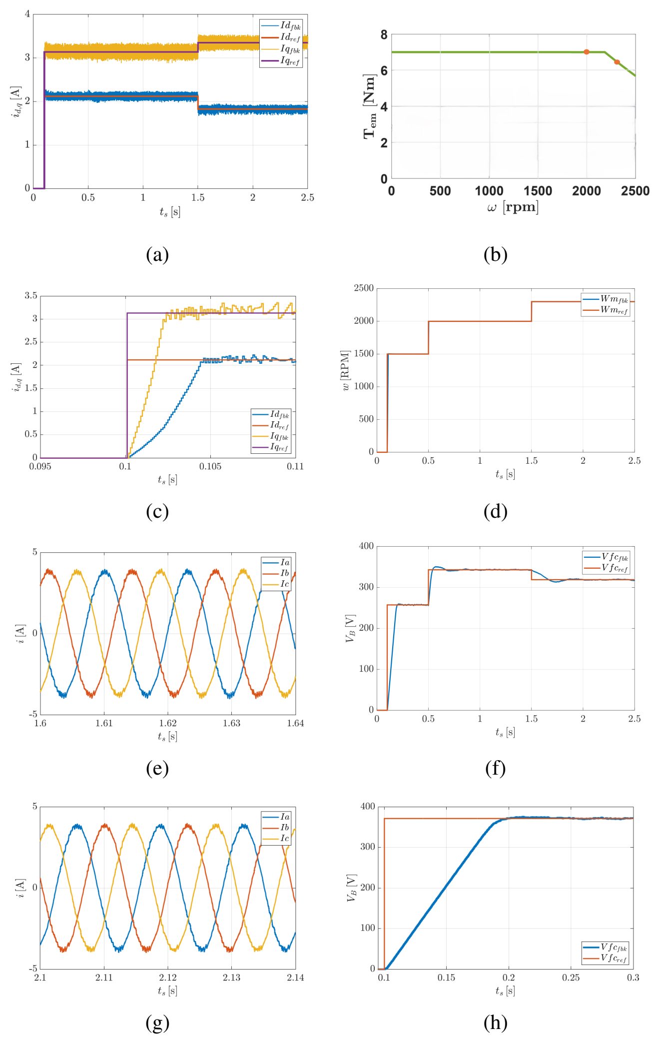

Fig. 7. (a) $i_d$,$i_q$ reference tracking. (b) $T\ vs\ w$ characteristic with tested points (i.e. 2000 rpm and 2300 rpm). (c) $dq$ current step tracking. (d) $w_m$ reference tracking. (e) $i_a$, $i_b$ and $i_c$ at steady state at 2000 rpm. (f) $V_B$ floating capacitor reference step. (g) $i_a$, $i_b$ and $i_c$ at steady state at 2300 rpm. (h) $V_B$ step tracking.

Thus, with $v_B^{p\,*}$ set to zero, the $dq$ reference values for the FC are:

$$V_{Bd}^{*} = -\frac{v_B^{q\,*} i_q^*}{|\bar{i}_S^*|} \tag{17a}$$

$$V_{Bq}^{*} = +\frac{v_B^{q\,*} i_d^*}{|\bar{i}_S^*|} \tag{17b}$$

The weighting factors $w_{V_B}$, $w_{V_{Bd}}$, and $w_{V_{Bq}}$ are scaling parameters determined through trial-and-error fashion to ensure consistency in the cost function units relative to the current errors.

## IV. Simulation Results

In this section, simulation results are shown to prove the effectiveness of the above-described control approach for an OEW-SyRel motor drive. The Main-Conv is fed by a constant voltage source at the rated voltage (i.e., 640 V), while the Aux-Conv floating capacitor voltage is directly controlled. The simulation setup involves controlling the current vector components and regulating the Aux-Conv dc-link voltage, while the rotational speed is managed by a prime mover. The performance of the $d$- and $q$-current reference tracking is depicted in Fig. 7(a), demonstrating the control system's ability to accurately follow the reference signals under varying conditions. Additionally, Fig. 7(c) offers a detailed view of the fast dynamic response of the current control, highlighting its capability to handle abrupt changes and maintain stability. Notably, the $q$-axis dynamic response is faster than the $d$-axis due to the smaller $L_{qq}$ inductance, resulting in a reduced time constant for the SyRel.

In addition to the current control, the FC voltage tracking performance is presented in Fig. 7(f), demonstrating the effectiveness of the control strategy in maintaining the desired voltage level. The corresponding step response, which emphasizes the transient behavior of the voltage control, is shown in Fig. 7(h). Notably, the dynamic performance of the FC-voltage control is slower than the current control. This characteristic highlights a key advantage of the predictive control approach, as it allows for the simultaneous management of state variables with different dynamic behaviors within a unified cost function—something that traditional PI controllers cannot achieve.

The rotational speed, which is set and controlled by the prime mover, is illustrated in Fig. 7(d). Starting from $t = 0.5$ s, the simulation includes the analysis of two significant operating points, labeled as the CTR region and the first flux-weakening in Fig. 7(b). These regions correspond to specific scenarios that test the control system's performance under different load and speed conditions. The torque limit curve shown in Fig. 7(b) is derived from the analysis presented in [11], considering an FC that extends the base speed compared to the standard SI case. During the first time interval ($0.5 < t < 1.5$ s), the current references $i_d^*$ and $i_q^*$ were set to the rated current, while the rotational speed was maintained at 2000 rpm, extending the base speed compared to the SI case, where the base speed is 1500 rpm. In the second time interval ($1.5 < t < 2.5$ s), the rotational speed was increased to 2300 rpm, allowing the system to enter the flux-weakening region. Fig. 8(a) and 8(c) illustrate a zero phase shift between the phase current $I_a$ and the voltage $Va_A$ at both 2000 rpm and 2300 rpm, respectively. Additionally, Fig. 8(b) and 8(d) show that the $a$-phase current and the corresponding phase voltage output of the auxiliary converter ($Va_B$) exhibit a 90° phase shift at both speeds. This observation demonstrates that the reactive power is fully compensated, with no active power exchanged between the motor and the auxiliary converter. The floating capacitor effectively supplies the entire system with reactive power, highlighting its proactive role in guaranteeing the unity power factor of the main converter DC link.

## V. Conclusions

This paper has presented an experimental magnetic characterization of the SyRel and an FCS-MPC for an OEW-SyRel

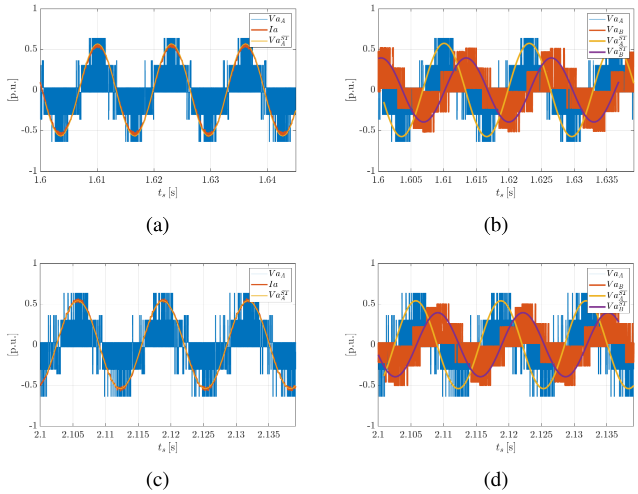

Fig. 8. Current and voltage waveforms for (a) Main-Conv at 2000 rpm. (b) Main-Conv and Aux-Conv at 2000 rpm. (c) Main-Conv at 2300 rpm. (d) Main-Conv and Aux-Conv at 2300 rpm.

drive. An FCS-MPC has been employed to control the system at the desired operating points. The FCS-MPC considerably simplifies the control design and two independent inverters can be driven by a single cost function. Simulation results outline the effectiveness of the proposed control that can achieve a unity power factor and torque reference tracking. Furthermore, the OEW-SyRel drive configuration enables extending torque-versus-speed characteristics when compared to the SI layout and increases the main converter power factor.


## ACKNOWLEDGMENT

This work was supported by the Marie Skłodowska-Curie Actions (MSCA) under the European Union's Horizon 2020 Research and Innovation Staff Exchange (RISE) under Grant 872001.


## REFERENCES


[1] M. Murataliyev, M. Degano, M. Di Nardo, N. Bianchi, and C. Gerada, "Synchronous reluctance machines: A comprehensive review and technology comparison," *Proceedings of the IEEE*, vol. 110, no. 3, pp. 382–399, 2022.

[2] N. Bianchi, S. Bolognani, E. Carraro, M. Castiello, and E. Fornasiero, "Electric vehicle traction based on synchronous reluctance motors," *IEEE Transactions on Industry Applications*, vol. 52, no. 6, pp. 4762–4769, 2016.

[3] A. Amerise, L. Rovere, A. Formentini, M. Mengoni, L. Zarri, and P. Zanchetta, "Electric drive based on an open-end winding surface PM synchronous machine with a floating capacitor bridge," *IEEE Transactions on Industry Applications*, vol. 56, no. 3, pp. 2709–2718, 2020.

[4] Y. Zuo, X. Zhu, X. Si, and C. H. T. Lee, "Fault-tolerant control for multiple open-leg faults in open-end winding permanent magnet synchronous motor system based on winding reconnection," vol. 36, no. 5, 2021, pp. 6068–6078.

[5] M. Zerdani, S. A. E. M. Ardjoun, H. Chafouk, and M. Denaï, "Experimental investigation of decoupled discontinuous pwm strategies in open-end winding induction motor supplied by a common dc-link," *IEEE Journal of Emerging and Selected Topics in Power Electronics*, vol. 11, no. 3, pp. 3087–3096, 2023.

[6] E. L. Soares, C. B. Jacobina, N. B. de Freitas, N. Rocha, A. C. N. Maia, and A. M. N. Lima, "A multilevel open-end winding six-phase induction motor drive topology based on three two-level three-phase inverters," *IEEE Transactions on Industry Applications*, vol. 59, no. 5, pp. 6360–6372, 2023.

[7] L. Rovere, G. Valente, A. Formentini, and P. Zanchetta, "Parameters and volt–ampere ratings of a floating capacitor open-end winding synchronous motor drive for extended CPSR," *IEEE Transactions on Industrial Electronics*, vol. 69, no. 5, pp. 4576–4586, 2022.

[8] L. Rovere, A. Formentini, G. L. Calzo, P. Zanchetta, and T. Cox, "Zero-sequence voltage elimination for dual-fed common dc-link open-end winding pmsm high-speed starter–generator—part i: Modulation," *IEEE Transactions on Industry Applications*, vol. 55, no. 6, pp. 7804–7812, 2019.

[9] X. Yuan, C. Zhang, and S. Zhang, "Torque ripple suppression for open-end winding permanent-magnet synchronous machine drives with predictive current control," vol. 67, no. 3, 2020, pp. 1771–1781.

[10] L. Wang, W. Huang, and F. Bu, "The reduction of zero-sequence voltage for open-end winding asynchronous motor driver with dual inverter," in *2017 20th International Conference on Electrical Machines and Systems (ICEMS)*, 2017, pp. 1–5.

[11] J. Riccio, F. Gemma, L. Rovere, G. Tresca, M. D. Nardo, S. Odhano, M. Degano, and P. Zanchetta, "Effects of the floating capacitor voltage on the torque-speed characteristic of an open-end winding synchronous reluctance motor drive," *IEEE Transactions on Industry Applications*, pp. 1–10, 2025.

[12] M. Mengoni, A. Amerise, L. Zarri, A. Tani, G. Serra, and D. Casadei, "Control scheme for open-ended induction motor drives with a floating capacitor bridge over a wide speed range," *IEEE Transactions on Industry Applications*, vol. 53, no. 5, pp. 4504–4514, 2017.

[13] Y.-F. Jia, N. Xu, L. Chu, Y. Zhang, Z. Xu, Y.-K. Li, and Z.-H. Yang, "Control strategy for an open-end winding induction motor drive system for dual-power electric vehicles," *IEEE Access*, vol. 8, pp. 8844–8860, 2020.

[14] P. Karamanakos and T. Geyer, "Guidelines for the design of finite control set model predictive controllers," *IEEE Transactions on Power Electronics*, vol. 35, no. 7, pp. 7434–7450, 2020.

[15] D. Minaglia, L. Rovere, A. Formentini, R. Leuzzi, S. Pipolo, M. Marchesoni, and P. Zanchetta, "Control of a dual fed open end winding spmsm with a floating capacitor," in *2020 IEEE Energy Conversion Congress and Exposition (ECCE)*, 2020, pp. 4036–4043.

[16] J. Riccio, P. Karamanakos, S. Odhano, M. Tang, M. D. Nardo, G. Tresca, and P. Zanchetta, "Modulated model-predictive integral control applied to a synchronous reluctance motor drive," *IEEE Journal of Emerging and Selected Topics in Power Electronics*, vol. 11, no. 3, pp. 3000–3010, 2023.

[17] E. Armando, R. I. Bojoi, P. Guglielmi, G. Pellegrino, and M. Pastorelli, "Experimental identification of the magnetic model of synchronous machines," vol. 49, no. 5, 2013, pp. 2116–2125.

[18] F. Gemma, J. Riccio, G. Tresca, A. Volpini, and P. Zanchetta, "Finite-control-set model predictive control with reduced computational burden in cascaded h-bridge permanent magnet synchronous motor drives for ev applications," in *2024 IEEE Energy Conversion Congress and Exposition (ECCE)*, 2024, pp. 3941–3947.

[19] J. Riccio, P. Karamanakos, S. Odhano, M. Tang, M. D. Nardo, and P. Zanchetta, "A direct model predictive control strategy for high-performance synchronous reluctance motor drives," in *2021 IEEE Energy Conversion Congress and Exposition (ECCE)*, 2021, pp. 4704–4710.